Applied Catalysis B: Environmental 218 (2017) 515–524

Contents lists available at ScienceDirect

Applied Catalysis B: Environmental

journal homepage: www.elsevier.com/locate/apcatb

Carbon vacancy regulated photoreduction of NO to N_2 over ultrathin g-C_3N_4 nanosheets

Guohui Dong[a,*], Daniel L. Jacobs[b], Ling Zang[b,*], Chuanyi Wang[a,*]

[a] School of Environmental Science and Engineering, Shaanxi University of Science and Technology, Xi'an 710021, China
[b] Nano Institute of Utah and Department of Materials Science and Engineering, University of Utah, Salt Lake City, UT 84112, United States

ARTICLE INFO

Article history:
Received 22 May 2017
Received in revised form 19 June 2017
Accepted 4 July 2017
Available online 5 July 2017

Keywords:
Graphitic carbon nitride
NO removal
Photoreduction
Carbon vacancy

ABSTRACT

Photocatalytic oxidation has recently been recognized as an attractive technology for NO removal, in which the main products are NO_2 or HNO_3. However, these products may cause secondary pollution and deactivation of the involved photocatalysts. In this study, we demonstrate that carbon vacancy-modified nanosheet structure g-C_3N_4 (Ns-g-C_3N_4) can efficiently and selectively reduce NO to N_2 under visible light. Since N_2 is a green gas and can easily desorb from the active sites, the problems such as secondary pollution and catalyst deactivation are largely avoided. It was found that two structural characters of Ns-g-C_3N_4, ultrathin nanostructure and abundant surface defect sites, could promote its visible light absorption, and favor the separation and transfer of photogenerated charge carriers as well as strong chemisorption of NO, leading to high photoreactivity. Meanwhile, the surface defects of Ns-g-C_3N_4 shift the adsorption structure of NO from C—N—O for the bulk counterpart to Cv—O—N (adsorbed at the carbon vacancy site, Cv), eventually resulting in its high selectivity of converting NO to N_2. The present study underlines the impetus of utilizing surface defect structure to regulate photocatalytic reaction pathway.

1. Introduction

Nitric oxide (NO) is one of the most common and dangerous gaseous pollutants which can cause environmental problems, such as haze, photochemical smog, and acid rain [1–3]. A major source of NO is through combustion, and since the increase of automobiles and industrial activities, the concentration of NO in the atmosphere has greatly increased over the past few decades [4,5]. Therefore, it is necessary to develop efficient, low cost and green technologies to remove NO from the atmosphere. Conventional NO removal methods include chemical adsorption, physical adsorption and thermal catalytic reduction [6–9]. However, most of these methods suffer from the problems of low efficiency, deactivation of catalyst, and secondary pollution. Semiconductor photocatalysis has recently been recognized as an attractive alternative technology for NO removal due to its high catalytic performance at moderate conditions and the abundant solar energy available [10]. In photocatalysis, light irradiation causes the bandgap excitation, producing electrons (e^-) and holes (h^+) located at valence and conduction band, respectively, which can then migrate to the surface and trigger subsequent redox reactions [11]. Through the redox reaction, NO can be eliminated effectively. It was reported that TiO_2, ZnO_2, and Fe_2O_3 could act as efficient photocatalysts for removing NO under UV light irradiation [12–14]. However, their intrinsic wide band gap nature makes these photocatalysts only active in UV region, which occupies only ~5% of sunlight. Therefore, it is essential to develop photocatalysts that are responsive to visible light (accounting for about 43% of sunlight). Many visible light-driven photocatalysts including $(BiO)_2CO_3$, BiOBr, Bi_2MoO_6, $InVO_4$ and graphitic carbon nitride (g-C_3N_4) have been developed and utilized for NO removal [15–20]. Among these materials, g-C_3N_4 has attracted increasing attention because of its stability, low cost, suitable band gap of 2.7 eV and surface flexibility for chemical modification [21]. We found that g-C_3N_4 could oxidize NO to NO_2 under visible light irradiation in our previous work [22]. However, NO_2 is an undesired product as it is more toxic than NO. Very recently, we demonstrated that the photooxidation product NO_2 could be further oxidized to NO_3^- by modifying g-C_3N_4 with Pd nanoparticles. Unfortunately, NO_3^- will occupy the active sites and cause the catalytic deactivation of g-C_3N_4 [23]. Therefore, it is of the utmost urgency but a challenge to design a route to remove NO without secondary pollution and catalytic deactivation.

Aside from NO_2 and NO_3^-, N_2 is also a possible product in the photocatalytic removal of NO. Since N_2 is a clean gas and can easily desorb from the active sites, the problems of deactivation

* Corresponding authors.
E-mail addresses: dongguohui@sust.edu.cn (G. Dong), lzang@eng.utah.edu (L. Zang), cywang@ms.xjb.ac.cn (C. Wang).

http://dx.doi.org/10.1016/j.apcatb.2017.07.010
0926-3373/

and secondary pollution can be largely avoided [24]. However, the conversion from NO to N_2 is very difficult because of high dissociation energy of N≡O triple bond (632 KJ/mol). Although it has been reported that TiO_2 can reduce NO to N_2 under UV light irradiation, the conversion efficiency is only 2% [24]. According to previous reports, chemical adsorption is critical to the reduction of gas molecules, such as O_2, CO_2 and N_2 [25–27]. It has been shown that the chemisorption mode of the gas molecules on the surface of catalyst can control either reaction path or the reaction products [25–28]. In general, chemisorption mode of gas molecules on a catalytic material depends on its surface structure [25–28]. This is due to the fact that different surface structures may have different atom terminations and surface energies. Thus, to alter the products of photocatalytic NO removal, the catalyst's surface structure would be an important factor to control.

Recent experimental studies have shown that two dimensional nanosheet materials possess unique surface structure, giving rise to enhanced photocatalytic performance compared to their bulk counterparts [29,30]. It is reasonable to consider that nanosheet structure of g-C_3N_4 may exhibit different behavior in photocatalytic NO conversion process than the bulk structured one. However, to the best of our knowledge, there lacks systematic study on the photocatalytic NO removal by nanosheet structured g-C_3N_4 under visible light. In this study, we report on a simple method of synthesizing ultrathin nanosheets of g-C_3N_4 and the application as photocatalyst for converting NO to N_2, for which the detailed structure of g-C_3N_4 nanosheet and photocatalytic mechanism were extensively investigated.

2. Experimental section

2.1. Preparation of catalysts

All chemicals used in this study were analytical-grade reagents without further purification. Nanosheet structure graphitic carbon nitride (Ns-g-C_3N_4) was synthesized by mixing melamine (1 g) with cyanuric acis (2 g) in 20 mL of ethanol with stirring at 333 K to remove the ethanol. The resultant mixture was put into an alumina crucible with a cover and then heated to 550 °C for 4 h in air to obtain the final samples. The bulk graphitic carbon nitride (g-C_3N_4) was prepared by heating melamine (3 g) in 20 mL of ethanol using the same heating procedures as just described.

2.2. Sample characterization

The crystal structures of the final samples were analyzed by Bruker D8 Advance X-ray diffractometer (XRD) with Cu Kα radiation at 40 KV and 40 mA. The morphology of the final samples was analyzed by transmission electron microscopy (TEM, JEOL JSM-2010). Surface electronic states were analyzed by X-ray photoelectron spectroscopy (XPS, Perkin-Elmer PHI 5000C, Al KR). All of the XPS spectra were calibrated to the C 1s peak at 284.6 eV of the surface adventitious carbon. Electron paramagnetic resonance (EPR) signals were recorded at room temperature (298 K) with a Bruker ESR A300 spectrometer. The UV–vis diffuse reflectance spectra (DRS) were obtained using a UV–vis spectrometer (Shimadzu UV-2550) by using $BaSO_4$ as a reference and were converted from reflection to absorbance by the Kubelka-Munk method. Photoluminescence spectra (PL) of the final samples were obtained using a fluorescence spectrometer (Hitachi F-4500) at 293 K. The nitrogen adsorption and desorption isotherms at 77 K were measured using Micrometrics ASAP2020 system after samples were vacuum dried at 180 °C overnight. Fourier transform infra red spectroscopy (FT-IR) spectra were obtained using a FT-IR spectrophotometer (Nicolet iS50, Thermo) with KBr as the reference sample.

2.3. Photocatalytic activity measurement

The experiments of photocatalytic NO removal on g-C_3N_4 and Ns-g-C_3N_4 were carried out in a continuous flow reactor. In the experiment, 50 mg of g-C_3N_4 or Ns-g-C_3N_4 was added to 10 mL of H_2O and ultrasonicated for 15 min. The aqueous suspension was then cast onto the glass dish (R = 3 cm), followed by drying at 60 °C until the water was completely removed. The glass dish was placed in the middle of the reactor. A 300 W Xe lamp with a 420 nm cut-off filter was vertically placed above the quartz window, so that the incident light can irradiate directly on the sample dish. Compressed NO (10 ppm, balance with Ar) was used as the NO source. NO concentration was diluted to about 600 ppb by air stream. The flow rate was controlled at 1 L/min by a mass flow controller. The change in NO concentration was continuously measured by using a chemiluminescence NO analyzer (Thermo Scientific, 42i).

NO removal efficiency (η) was calculated as follows:

$$\eta(\%) = (1-[NO]_f/[NO]_i) \times 100\%$$

where $[NO]_f$ and $[NO]_i$ are the concentrations of NO in the outlet stream and feeding stream, respectively.

2.4. Anaerobic photocatalytic NO removal

In the anaerobic photocatalytic NO removal, a 0.1 g amount of photocatalyst was uniformly dispersed on a glass reactor with an area of 4.2 cm^2. The volume of the reaction system was about 230 mL. The reaction setup was vacuum-treated several times, and then 1500 ppb NO (Banlance with Ar) was introduced into the reaction to achieve ambient pressure. During the irradiation, about 1 mL of gas was taken from the reaction cell at given intervals for subsequent N_2 concentration analysis with a gas chromatograph (GC-14B, Shimadzu Corp., Japan).

The selectivity of N_2 (S_{N2}) was calculated as follows:

$$S_{N2} = ([N_2]/[N_2] + [NO_2]) \times 100\%$$

2.5. Electrochemical and photoelectrochemical experiments

Electrochemical and photoelectrochemical measurements were performed in a three-electrode cell with a platinum plate (1 × 1 cm^2) as the auxiliary electrode and a saturated calomel electrode (SCE) as the reference electrode on a CHI 660C workstation. The working electrode (photoelectrode) was immersed in a 0.1 M KCl aqueous solution. Time dependent photocurrent curves were measured with amperometric i–t curve method. A 300 W Xe lamp with a 420 nm cutoff filter was chosen as a visible light source. Nyquist plots were obtained by using the AC impedance method.

The photoelectrodes were prepared as described in our previous report [31]. Typically, the aqueous slurries of g-C_3N_4 and Ns-g-C_3N_4 were spin-coated on ITO glass substrate at a spin rate of 3000 rpm for 30 s under low vacuum. The films on ITO glass substrate were dried in air and annealed at 200 °C for 1 h as the final photoelectrodes.

3. Results and discussion

3.1. Structure characterization for samples

The microstructures of the result samples were investigated by transmission electron microscopy (TEM). Fig. 1a shows that the bulk g-C_3N_4 sample synthesized with only melamine is of a multilayer structure. Alternatively, when the mixture of melamine and cyanuric acid was used as precursor, the resulting Ns-g-C_3N_4 sample was composed of ultrathin nanosheets with a thickness of 10 nm

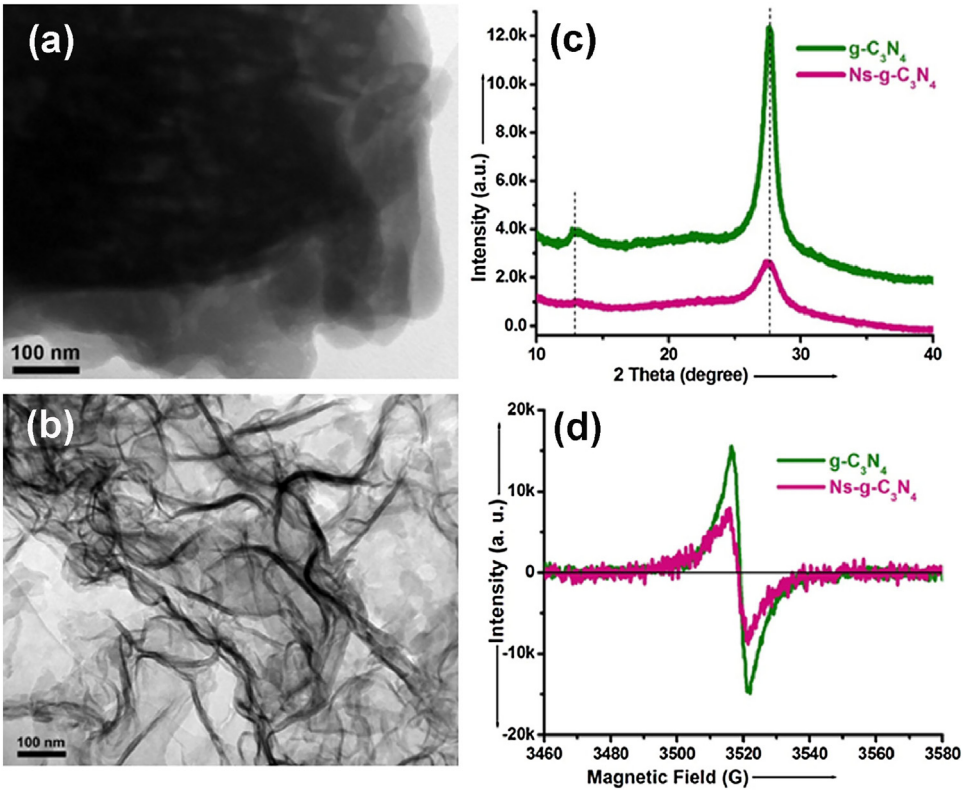

Fig. 1. TEM image of g-C_3N_4 (a) and Ns-g-C_3N_4 (b). XRD patterns of g-C_3N_4 and Ns-g-C_3N_4 (c). EPR patterns of g-C_3N_4 and Ns-g-C_3N_4 (d).

(Fig. 1b). The crystal structures of the two samples were compared by X-ray diffraction (XRD) measurements (Fig. 1c). Both the two samples contain two peaks at about 13.0° and 27.4°, matching well with the (100) and (002) crystal planes of g-C_3N_4, respectively. No other impurity peaks can be detected in the XRD pattern of Ns-g-C_3N_4, indicating that the co-calcination with cyanuric acid does not affect the crystal structure of the graphite-like carbon nitride. However, the peak at 27.4° of Ns-g-C_3N_4 is weaker, suggesting that the interlayer structure of g-C_3N_4 has been weakened, which agrees well with the change in the micro-morphology. Previous work suggested that nanosheets may contain additional surface defect sites compared to their bulk counterparts [29]. It is therefore reasonable to speculate that the surface of Ns-g-C_3N_4 prepared in this study also contain such defects. To test this hypothesis, electron paramagnetic resonance (EPR) spectrometry was used to detect the presence of defects. Fig. 1d shows that the bulk g-C_3N_4 exhibits a Lorentzian line originating from the unpaired electrons on the carbon atoms of the aromatic rings [26]. In Ns-g-C_3N_4, this line is considerably damped, which signifies a reduction in the number of unpaired electrons, likely due to the formation of carbon vacancies.

To understand this proposed defect formation, X-ray photoelectron spectroscopy (XPS) was employed to investigate the surface chemical composition and chemical states of the two g-C_3N_4 samples. High-resolution XPS peaks of C 1*s* of the two samples can be deconvoluted into two peaks, which are ascribed to the carbon in C—N_3 (288.2 eV) and C—C (284.6 eV, arising from the adventitious carbon) groups, respectively (Fig. 2a). The area ratios of the two peaks at 288.2 and 284.6 eV are calculated to be 2.7 and 1.6 for g-C_3N_4 and Ns-g-C_3N_4, respectively. This decrease in area ratio suggests that the tertiary carbon content in Ns-g-C_3N_4 is decreased, which in turn suggests an increase in carbon vacancies. Moreover, the high-resolution XPS peaks of N 1*s* of g-C_3N_4 can be fitted with two peaks, which are ascribed to the C—N—C (398.4 eV) and C—N_3 (400.7 eV) groups, respectively. However, in addition to these two peaks, a new peak, which is attributed to the amino groups (-NH_2, 401.3 eV), was observed in the high-resolution XPS spectra of Ns-g-C_3N_4 (Fig. 2b). The formation of amino groups is in consistence with the decrease in tertiary carbons, further implying the formation of carbon vacancies.

3.2. Photocatalytic NO removal

The photocatalytic activities of the two g-C_3N_4 samples were examined for the NO removal preformed in a continuous flow reactor system. Inlet NO concentrations were 600 ppb flowing at a constant rate of 1 L/min. Experimental details can be found in the supporting information. Control experiments showed that there was no observable NO removal in the absence of either the photocatalyst or visible light irradiation (Fig. 3a), indicating that both the photocatalyst and visible light are necessary for the present photocatalytic NO removal. Fig. 3a shows that 38% of NO could be removed over bulk g-C_3N_4 under visible light irradiation (>420 nm) for 40 min. In comparison, Ns-g-C_3N_4 shows significantly improved photocatalytic activity with 48% of NO removed in only 30 min under the same visible light irradiation. The NO concentration change follows first-order kinetics, and the NO removal rate over Ns-g-C_3N_4 is 5 times of that over g-C_3N_4 (Fig. 3b). Since the removal of NO can be either through a reduction pathway to N_2, or an oxidation way to NO_2, we first studied the reaction process by monitoring the production of NO_2, as well as the concentration change. For the bulk g-C_3N_4, a large amount of NO_2 was produced (with yield percentage of 80%) after 30 min of visible light irradiation, suggesting that the major photocatalytic product in this case was NO_2 (Fig. 3c). However, when the ultrathin nanosheets of g-C_3N_4 were used as the photocatalyst, the concentration of NO_2 generated was much lower (with yield percentage of 33%). One possibility accounting for this difference is that Ns-g-C_3N_4 may facilitate deep oxidation of NO to NO_3^- or NO_2^-, decreasing the formation of NO_2. Con-

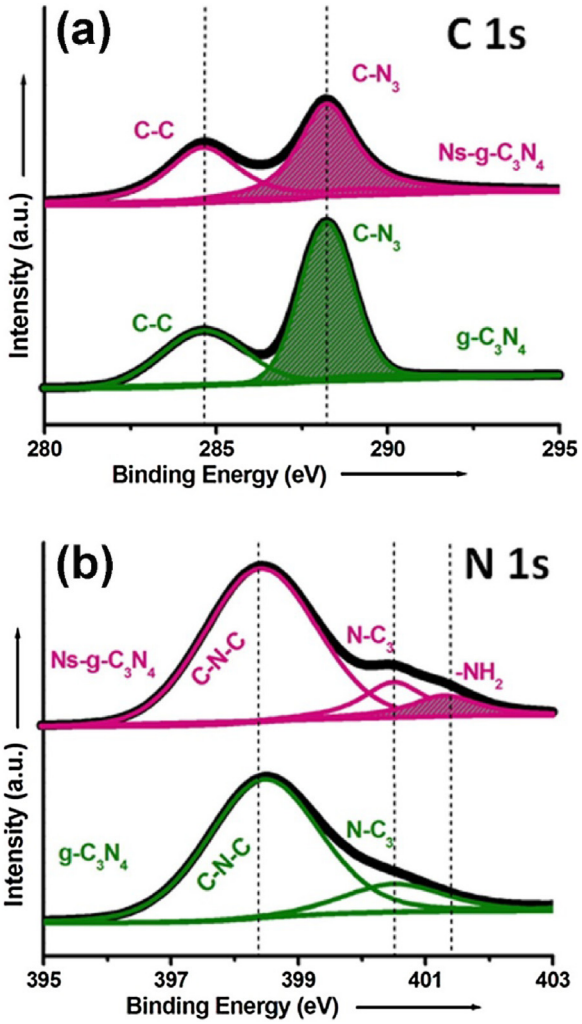

Fig. 2. High-resolution XPS spectra of C 1s (a) and N 1s (b) of g-C_3N_4 and Ns-g-C_3N_4.

sidering the strong adsorption of NO_3^- or NO_2^- on the surface of g-C_3N_4, we should be able to detect the presence of these ions if the deep oxidation indeed occurred. However, FTIR measurement over the Ns-g-C_3N_4 sample collected after the photocatalytic reaction found no peaks corresponding to NO_3^- or NO_2^- (Fig. 3d). This implied that significant amount of NO must have gone through a different reaction process over Ns-g-C_3N_4, and been converted to a different product.

In order to explore the reaction pathways in Ns-g-C_3N_4 system, trapping experiments were carried out to investigate and compare photocatalytic removal of NO. When potassium iodide (KI, a hole scavenger) [32] was added into the materials, the NO removal was completely inhibited over g-C_3N_4 (Fig. S1a), whereas the NO removal over Ns-g-C_3N_4 was reduced by only 30%. This observation implies that photogenerated holes are indispensable for NO removal over g-C_3N_4 but not for Ns-g-C_3N_4. On the other hand, with addition of potassium dichromate ($K_2Cr_2O_7$, an electron scavenger) [33] the NO removal was significantly depressed for both g-C_3N_4 and Ns-g-C_3N_4 (Fig. S1a and S1b), suggesting that the photogenerated electrons play a critical role in NO removal in both cases. In the presence of oxygen, the photogenerated electrons can form various active species participating in the catalytic response. To probe this, scavengers such as tert-butyl alcohol (TBA) for ·OH, p-benzoquinone (PBQ) for $\cdot O_2^-$ and catalase (CAT) for H_2O_2 were further tested on the photocatalytic response [34–36]. As shown in Figs. S1a and S1b, the addition of TBA and CAT did not change the NO removal rate over both g-C_3N_4 and Ns-g-C_3N_4. On the contrary, PBQ could depress the NO removal on both samples. Interestingly, the NO removal efficiency of both samples in the presence of PBQ was almost equal to that in the presence of KI. Thus, we conclude that both the photogenerated hole and $\cdot O_2^-$ are indispensable, playing the synergic roles, in the NO removal over g-C_3N_4. However, the NO removal over Ns-g-C_3N_4 is attributed not only to the synergic roles of hole and $\cdot O_2^-$, but also to other more important contributions related to the electrons.

Based on the importance of photogenerated electrons on the NO removal mechanism, as well as the unaccounted for product of NO reduction evidenced by the suppression of NO_2 formation in the Ns-g-C_3N_4 system, a photoreduction mechanism is proposed. It has been reported that oxygen vacancies in TiO_2 lead to selective reduction of NO into N_2 under UV light irradiation [24]. Similarly, in this work, the carbon vacancy within the surface of Ns-g-C_3N_4 would also lead to the reduction of NO under visible light irradiation. To prove this, the compressed air carrier gas was replaced with high-purity argon gas to achieve anaerobic testing conditions. The results are shown in Fig. 4. NO removal on g-C_3N_4 is completely suppressed (Fig. 4a), suggesting that molecular oxygen was involved in NO removal with g-C_3N_4. However, the NO removal in Ns-g-C_3N_4 was only reduced by 34% (Fig. 4b) compared to the test in air, suggesting that oxygen is not indispensable for NO removal over Ns-g-C_3N_4. Gas chromatography (GC) measurements were carried out to identify the products of the anaerobic photocatalysis with

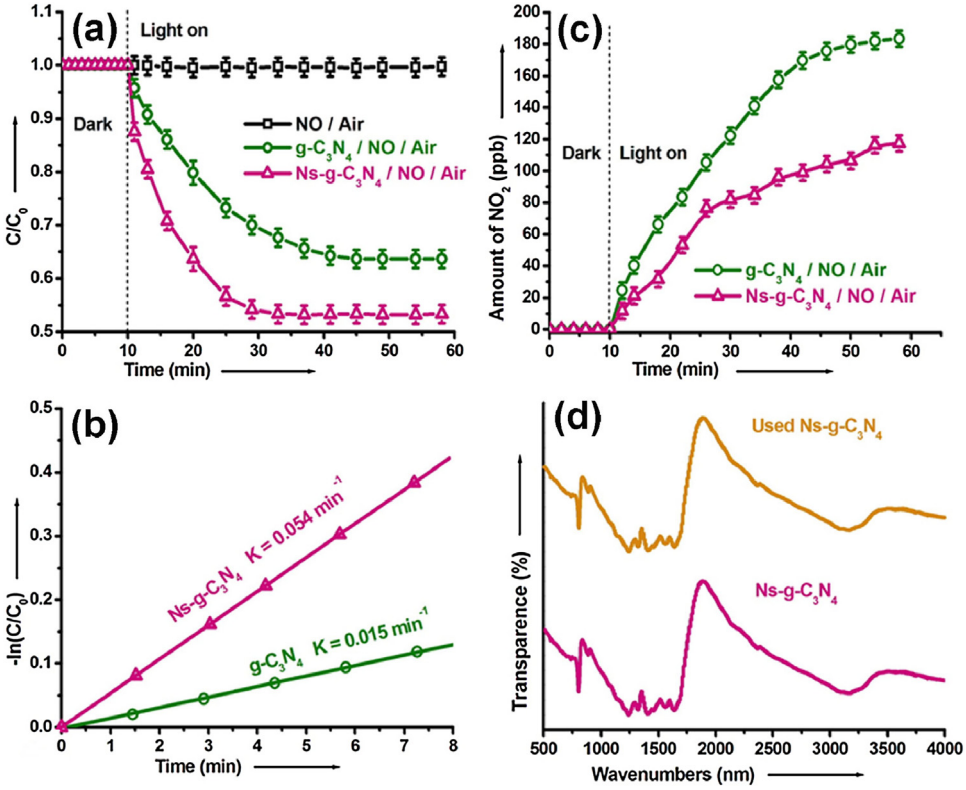

Fig. 3. (a) The relative change of NO concentration (C/C_0) as a function of irradiation time tested over g-C_3N_4 and Ns-g-C_3N_4. (b) First order kinetics fitting for the data obtained from g-C_3N_4 and Ns-g-C_3N_4. (c) NO_2 concentration changing with irradiation time tested over g-C_3N_4 and Ns-g-C_3N_4. (d) The FTIR spectra of Ns-g-C_3N_4 before and after used in photocatalytic removal of NO.

Ns-g-C_3N_4, and the GC spectra measured from the outlet gas of the reaction system is shown in Fig. 5b, where the formation of O_2 and N_2 is clearly evidenced. The area the O_2 to N_2 peaks in the GC spectra shows a 1:1 ratio, different from what is measured in the air sample (Fig. 5a). The 1:1 ratio is expected for the stoichiometric reduction of NO. Alternatively, no observable N_2 or O_2 peaks were seen with the g-C_3N_4 samples after 1 h of visible light irradiation (Fig. 5c). In addition, no N_2 and O_2 were detected over Ns-g-C_3N_4 when the photocatalytic system was illuminated by introducing Ar instead of NO/Ar into the reactor. These observations provide strong evidence that NO was reduced into N_2 and O_2 over Ns-g-C_3N_4. Based on the results of Fig. 5c, the selectivity of N_2 was calculated to be 66% for Ns-g-C_3N_4. To the best of our knowledge, this is the highest selectivity of N_2 in photocatalytic NO removal under the visible light irradiation [24].

3.3. *The mechanism of activity enhancement*

Photocatalytic NO removal starts with absorption of light energy, which in turn generates electrons and holes, causing surface reactions with NO. The photogeneration of electrons strongly depends on the band structure of the semiconductor catalyst. UV–vis absorption spectra of g-C_3N_4 and Ns-g-C_3N_4 are displayed in Fig. 6. The intrinsic direct band edge of Ns-g-C_3N_4 shows a slight blue shift compared with g-C_3N_4 (Fig. 6a); the g-C_3N_4 band gap of 2.7 eV increased to 2.8 eV for Ns-g-C_3N_4 (Fig. 6b). These changes are related to the quantum confinement effect (QCE), which is caused by the exfoliation in our system. At the same time, the absorption spectrum of Ns-g-C_3N_4 extends to the whole visible light region, possibly due to excitation into the lower energy defect states. In such case, Ns-g-C_3N_4 would absorb more visible light than g-C_3N_4, thereby generating more charges.

The photogenerated charges may undergo two fates: one is to migrate to the surface of the photocatalyst for subsequent chemical reactions; the other is to recombine with each other. The distance between the excitation sites and the surface depends on the morphology of the semiconductors. The morphology change from multi-layer structure to ultrathin nanosheets would shorten the distance for the photogenerated electrons to reach the surface, thus faciliating the charge separation. Additionally, our previous works revealed that carbon vacancies have the ability to capture electrons and suppress the radiative recombination of the photogenerated charges [26]. Therefore, the photogenerated electrons and holes are likely separated more efficiently in Ns-g-C_3N_4 than in g-C_3N_4. To test this, photoluminescence (PL) measurements were performed to study the separation of photogenerated electrons and holes in g-C_3N_4 and Ns-g-C_3N_4. Fig. 6c displays the PL spectra of the two samples under 330 nm excitation at room temperature. The strong emission peak of g-C_3N_4 around 455 nm was derived from the direct band transition. By contrast, the PL intensity of Ns-g-C_3N_4 was more than 50% lower, indicating the higher efficiency in separation of the photogenerated charge carriers. Moreover, beside the PL peak at 455 nm intrinsic to g-C_3N_4, a new band appeared at long wavelength in the PL spectrum of Ns-g-C_3N_4 sample, which may be due to radiative recombination from the shallow trapped electrons, likely at the carbon vacancies.

Electrochemical tests were performed in a three-electrode cell with a g-C_3N_4 coated working electrode to further understand the dynamics of electron transfer at the g-C_3N_4 surface. Fig. 6d shows the current of the electrochemical cell with pulsed light excitation. Under light illumination, both g-C_3N_4 and Ns-g-C_3N_4 generated significant photocurrent, implying efficient photogeneration of charge carriers in both materials that then transferred to the working electrode. Interestingly, the Ns-g-C_3N_4 system showed a lower photocurrent compared to the g-C_3N_4 system despite

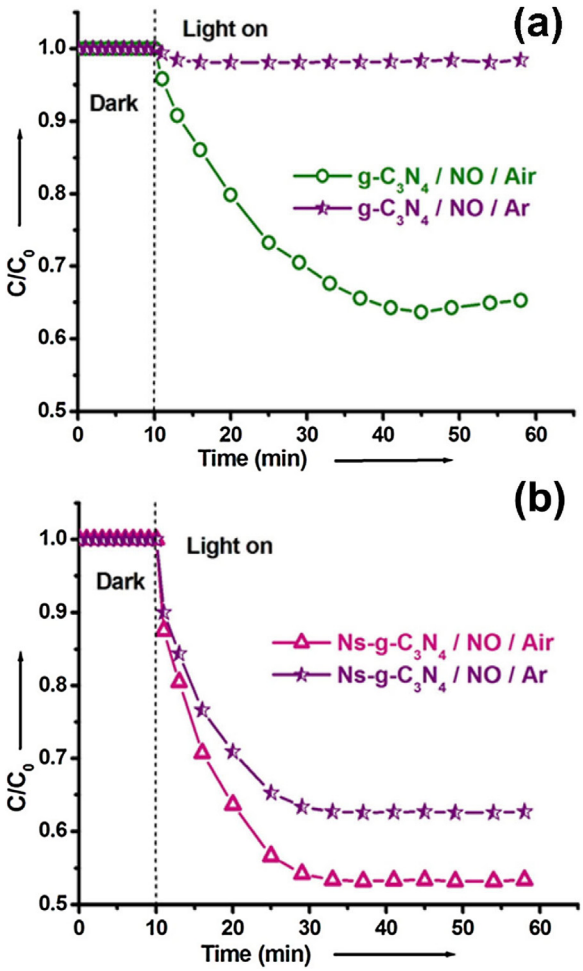

Fig. 4. Comparison of NO removal over g-C_3N_4 under aerobic and anoxic condition (a); Comparison of NO removal over Ns-g-C_3N_4 under aerobic and anoxic condition (b).

having larger light absorption and higher efficiency of charge separation as discussed above, which combined should result in a higher photocurrent. Therefore, it is expected that the charge transfer to the working electrode and/or the electrolyte in Ns-g-C_3N_4 system is inhibited due to the surface defects of carbon vacancy. Reduction of Cr(VI) via the photocatalysis was performed to measure the charge transfer properties at the surface. Indeed Ns-g-C_3N_4 exhibits lower reactivity in the photoreduction of Cr(VI), whose activity is merely 22% that of g-C_3N_4 (Fig. 6e), despite the higher surface area and expected larger photogenerated carrier concentrations of Ns-g-C_3N_4. These results, in consistence with the PL measurement above, indicate that the shallow level electron trapping (likely caused by carbon vacancies) inhibits the electron transport from the surface of Ns-g-C_3N_4. This is further confirmed by the measurements of electrochemical impedance shown in Fig. 6f. The Nyquist plots of the two samples show that the semicircle in the plot of Ns-g-C_3N_4 is larger than that of g-C_3N_4, indicating an increase in the charge transfer resistance on the surface. Based on all these experimental results, it can be concluded that Ns-g-C_3N_4 can produce more photoelectrons than g-C_3N_4, though the electrons generated are favorably trapped at the carbon vacancy sites.

The conclusion made above that the photogenerated electrons are confined in defects does not sound consistent with the fact that Ns-g-C_3N_4 exhibited higher reactivity in the photoreduction of NO to N_2. Such inconsistency can be explained by the different adsorption modes of the reactants on the surface of g-C_3N_4 and Ns-g-C_3N_4, which in turn affect the reaction rate and mechanism of the photocatalysis. Herein the adsorption of NO on g-C_3N_4 and Ns-g-C_3N_4 was extensively investigated in order to understand the effect on the photocatalytic activity. First, temperature-programmed desorption (TPD) of NO was investigated as displayed in Fig. S2. For g-C_3N_4, a single peak at 267 °C was observed, compared to two peaks at 267 °C and 370 °C for Ns-g-C_3N_4. The common peak at 267 °C is much weaker in the Ns-g-C_3N_4 sample, suggesting that the new strong adsorption mode at 370 °C is the dominant adsorption mode for NO on Ns-g-C_3N_4. This new strong adsorption mode is likely the source for the efficient photoreduction of NO on Ns-g-C_3N_4.

As previously reported, the nitrogen atom of NO has an unpaired electron, making it behave as a free radical. Meanwhile, the C atom in g-C_3N_4 also has an unpaired electron (Fig. S3a). Thus, the N atom of NO can interact with the C atom in g-C_3N_4 via radical coupling (Fig. S3b). Based on the results of EPR and XPS, the Ns-g-C_3N_4 defects are located on the C atoms, and the original free radical property of C atom may disappear. In addition, previous studies showed that the vacancies could act as the capture centers for O_2 molecules or the oxygen end of NO molecules [24,26]. As a result, the carbon vacancy of Ns-g-C_3N_4 may prefer to interact with the O atom rather than N atom. To confirm this change in NO adsorption modes, EPR measurement was conducted to compare the samples before and after NO adsorption. As shown in Fig. 7a, both g-C_3N_4 samples with and without NO adsorption show a sharp signal which could be assigned to the unpaired electrons on the carbon atoms in the aromatic rings. Interestingly, the signal intensity of g-C_3N_4 with the NO adsorption is lower than that without the NO adsorption. This is due to the fact that N atom of NO can interact with the C atom

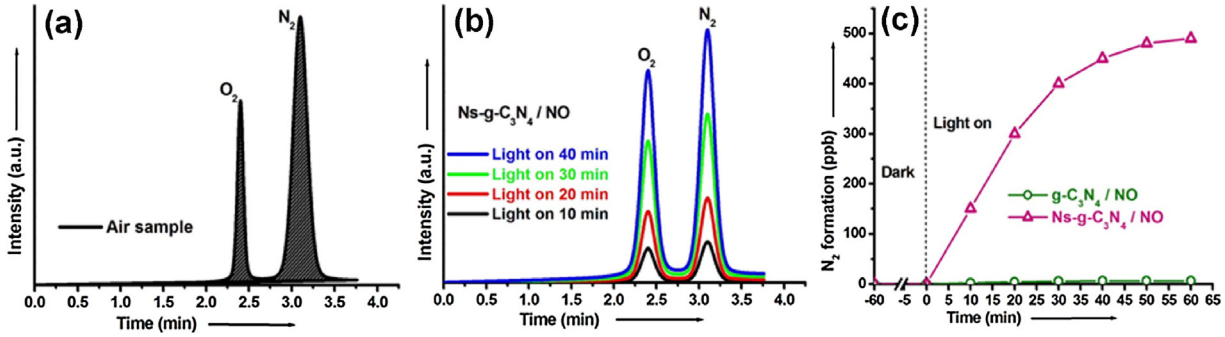

Fig. 5. The GC spectrum of air sample (a); The GC spectra of NO after the photocatalysis (b); photocatalytic conversion of NO to N_2 and O_2 over g-C_3N_4 and Ns-g-C_3N_4 (c). In anaerobic experiments, initial concentration of NO was 1500 ppb, the amount of g-C_3N_4, and Ns-g-C_3N_4 used was 50 mg, a 300 W Xe lamp with a 420 nm cutoff filter was used as the visible light source.

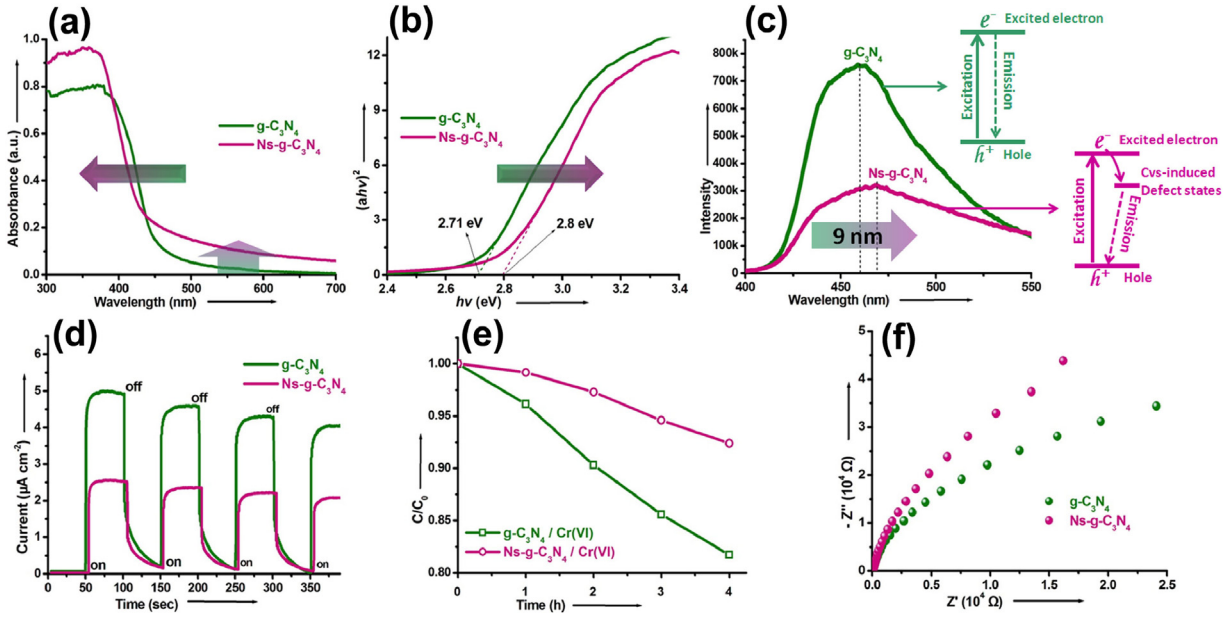

Fig. 6. UV–vis absorption spectra of g-C_3N_4 and Ns-g-C_3N_4 (a); the plots of $(ahv)^2$ versus energy (hv) of g-C_3N_4 and Ns-g-C_3N_4 (b); Photoluminescence spectrum of the g-C_3N_4 and Ns-g-C_3N_4 (c); The light dependent electrochemical current using g-C_3N_4 and Ns-g-C_3N_4 coated working electrodes(d); photoreduction of Cr(VI) over g-C_3N_4 and Ns-g-C_3N_4 (e); electrochemical impedance spectra of g-C_3N_4 and Ns-g-C_3N_4 (f).

in g-C_3N_4, thus decreasing the amount of the unpaired electrons in g-C_3N_4. The observation confirms the radical coupling mechanism of NO onto g-C_3N_4 surfaces as proposed above. The radical coupling driven adsorption is also supported by density functional theory (DFT) simulations. To simulate the molecular NO adsorption on surface of g-C_3N_4, a 3×3 supercell with a 15 Å vacuum thickness was used. Before surface energy optimization (Fig. 7b), NO molecules were located in the vacuum layer randomly. However, after the optimization, NO approaches the nearest C atom and results in σ bonding between N atom and C atom. This adsorption dynamic simulation is consistent with the result shown in Fig. 7a. As mentioned before, the ESR signal intensity of Ns-g-C_3N_4 is lower than that of g-C_3N_4 because of the increase in carbon vacancies. However, after NO pre-adsorption, its signal intensity increases to the same level as that of pristine g-C_3N_4 (Fig. 7c). This ESR change of Ns-g-C_3N_4 is contrary to that of g-C_3N_4, suggesting that carbon vacancy can serve as an active site to adsorb NO through interaction with the O atom of NO, leaving the radical at the N-atom, which results in an increase in the ESR signal of Ns-g-C_3N_4 sample.

To further confirm that the carbon vacancies on the Ns-g-C_3N_4 surface are the chemical adsorption sites for NO, these defect sites were intendedly blocked with photodeposition of Pd. Considering that photogenerated electrons are favorably confined in the defect sites, the particles of Pd can be selectively deposited on the defect sites through in situ photocatalytic reduction (Fig. 8). It is well known that NO can be adsorbed on the surface of Pd through the interaction between N atom and Pd [37]. Therefore, when the defects are blocked with Pd particles, the surface adsorption of NO will be dominated by the mode between N atom and Pd, whereas the mode based on interaction between carbon vacancy the O atom of NO will diminish, thus losing the ESR signal enhancement as observed for the pristine Ns-g-C_3N_4 sample. Indeed as shown in Fig. 8, for Pd modified Ns-g-C_3N_4 the NO pre-adsorption does not increase the ESR signal.

The results above reveal that the carbon vacancies on Ns-g-C_3N_4 serve two roles in the photocatalytic NO reduction. First, the carbon vacancies serve as traps for the photogenerated electrons, and this was supported by the electrochemical analysis shown in Fig. 6d and e. Second, the carbon vacancies provide preferential adsorption sites for NO. The localization of both the photogenerated electron and NO molecule to the same site allows for efficient reduction of NO through direct electron transfer. This direct electron transfer is supported by the decrease in PL intensity with increasing concentration of NO in Ar carrier gas as seen in Fig. 9. In contrast,

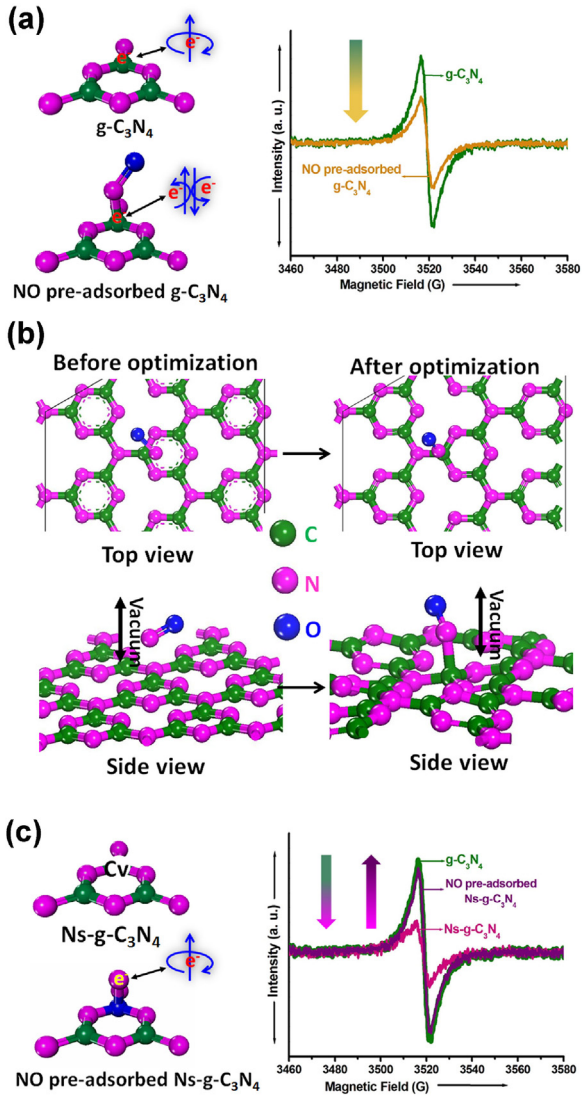

Fig. 7. The effect of the pre-adsorption of NO on the EPR spectrum of g-C_3N_4 and Ns-g-C_3N_4.

g-C_3N_4 does not exhibit any change in PL under the same conditions, confirming that there is no direct charge transfer between NO and g-C_3N_4. The direct charge transfer also explains the higher efficiency and conversion rate of NO in the Ns-g-C_3N_4 system compared to the bulk g-C_3N_4.

All in all, a possible pathway of photocatalytic reduction of NO over Ns-g-C_3N_4 is proposed. The first step would be the adsorption of NO on surface of Ns-g-C_3N_4 through the Cv—O—N interaction. The O—N single bond of Cv—O—N is then interrupted by the photogenerated electrons, thereby releasing the decomposed N and O. The decomposed N or O atoms react with each other and form the N_2 and O_2. To test this possibility, in situ ESR spectral measurement was conducted on pristine Ns-g-C_3N_4 and NO pre-adsorbed Ns-g-C_3N_4. As shown in Fig. 10, both samples with and without NO pre-adsorption show a sharp signal. When Ns-g-C_3N_4 sample was irradiated with visible light, the corresponding ESR signal showed an obvious increase, due to photogeneration of electrons (Fig. 10a). However, the visible light irradiation does not increase the ESR signal of NO pre-adsorbed Ns-g-C_3N_4. Additionally, the EPR peak of NO pre-adsorbed Ns-g-C_3N_4 shows a shift after the irradiation with visible light, implying that the kind of defect in NO pre-adsorbed Ns-g-C_3N_4 has changed. Moreover, the visible light irradiation on NO pre-adsorbed Ns-g-C_3N_4 leads to the appearance of two new ESR signals with the magnetic field of 3535 and 3555, respectively (Fig. 10b). These two signals can be attributed to the decomposed N and decomposed O [38,39]. This unambiguously proves the reduction pathway of NO over Ns-g-C_3N_4 as proposed above (Fig. 10c). To investigate the stability of Ns-g-C_3N_4, we conducted a recycling test for NO removal as shown in Fig. S4. No significant change in NO removal activity was found after four cycles, confirming that the active sites are not poisoned in the NO photoreduction process. This result can also be reflected in the Gas chromatography (GC) measurements because the area of O_2 to N_2 peaks shows a 1:1 ratio (Fig. 5b), implying no oxygen end or nitrogen end of NO was left on the surface of Ns-g-C_3N_4 after the NO removal. Moreover, the structure analysis of used Ns-g-C_3N_4 was also explored. Compared with XRD, EPR and XPS of initial Ns-g-C_3N_4, no significant changes can be found in XRD, EPR and XPS of used one (Fig. S5), indicating the structure of Ns-g-C_3N_4 is stable during photocatalytic NO removal.

4. Conclusions

In conclusion, we successfully fabricated ultrathin Ns-g-C_3N_4 nanosheets and investigated its photocatalytic properties with NO gas removal. Compared with g-C_3N_4, Ns-g-C_3N_4 exhibits higher conversion efficiency and conversion rate of NO. While g-C_3N_4 results in exclusive photoxidation of NO to NO_2, Ns-g-C_3N_4 also enables photoreduction of NO to N_2. It was found that the excellent photocatalytic activity of Ns-g-C_3N_4 is due to the existence of carbon vacancies at the surface compared to the bulk g-C_3N_4. These vacancy defects acted as electronic traps to localize the photogenerated electrons, while also serving as adsorption sited for NO through interface binding of Cv—O—N. The localization of both the photogenerated electron and NO molecule to the same site leads to the direct electron transfer from vacancy defect to NO, resulting in reduction of NO to N_2 and O_2. The direct electron transfer also explains the higher efficiency and conversion rate of NO photoreduction on Ns-g-C_3N_4 compared to that on bulk g-C_3N_4. The present work not only provides a new strategy towards achieving NO photoreduction at semiconductors, but also gives insight in molecular level understanding of the relationship between surface defect chemistry and the photocatalytic pathways of NO conversion. Lastly, to the regard of environmental impact, this work introduces an efficient and inexpensive method to remove harmful ambient NO pollution by converting it into environmentally benign N_2 gas, bringing a new way to use solar energy to solve air pollution.

Acknowledgments

Financial support by the National Nature Science Foundation of China (Grant No. 21603271 and 21473248), NSF (CBET 1502433) and the CAS/SAFEA International Partnership Program for Creative Research Teams is gratefully appreciated.

Appendix A. Supplementary data

Supplementary data associated with this article can be found, in the online version, at http://dx.doi.org/10.1016/j.apcatb.2017.07.010.

The photoreduction of Cr(VI) in the presence of different photocatalysts under visible light; the influence of different scavengers on the photocatalytic removal of NO; NO TPD spectra of g-C3N4 and Ns-g-C3N4; Repeated testing of NO removal over Ns-g-C3N4.

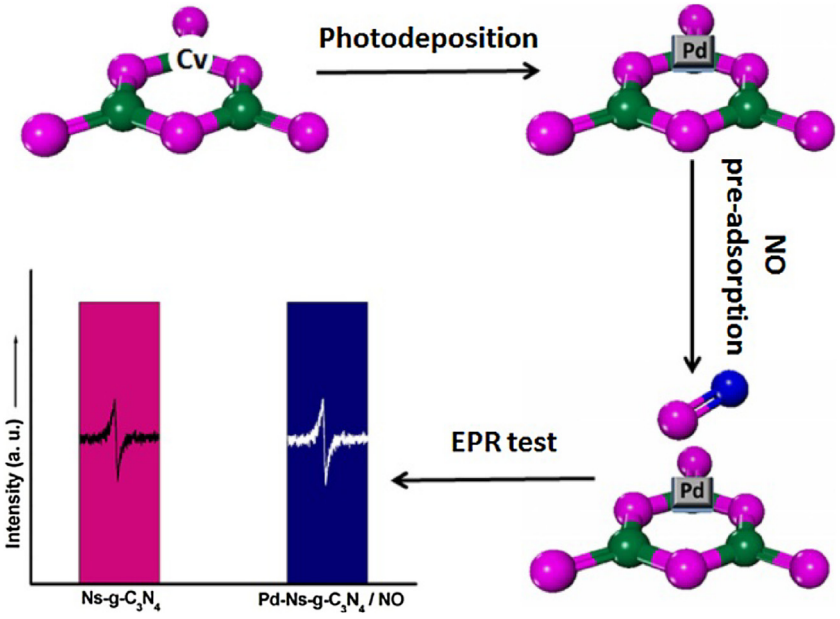

Fig. 8. The effect of the Pd on the NO adsorption on Ns-g-C_3N_4.

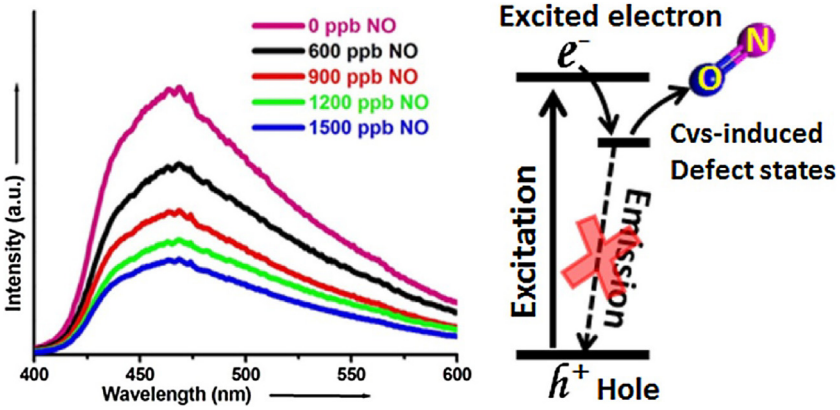

Fig. 9. The effect of the NO on the Photoluminescence spectrum of Ns-g-C_3N_4.

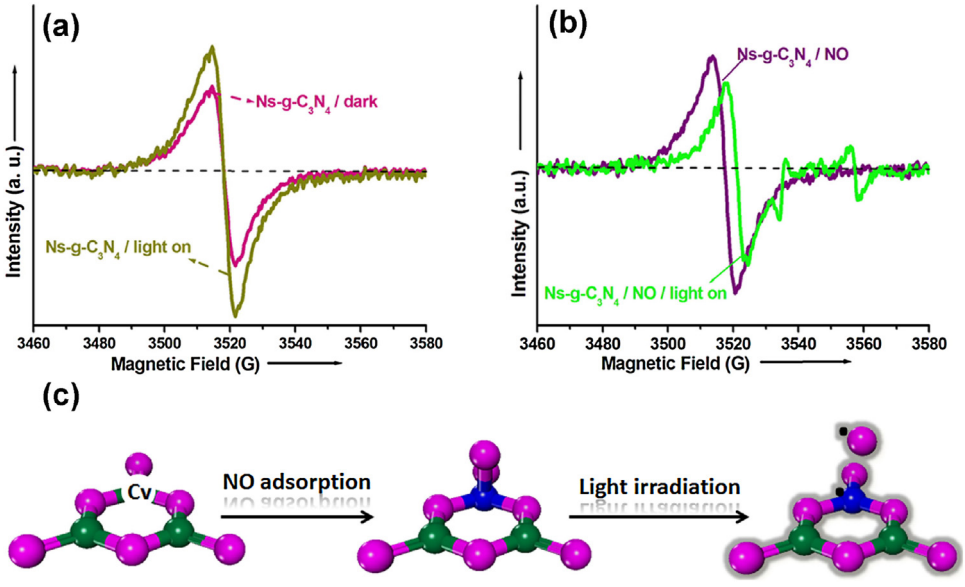

Fig. 10. The effect of the light irradiation on the EPR spectrum of Ns-g-C_3N_4 (a) and NO pre-adsorbed Ns-g-C_3N_4 (b); the decomposition process of NO on the surface of Ns-g-C_3N_4 (c).

References

[1] M.T. Lerdan, J.W. Munger, D.J. Jacob, The NO_2 flux conundrum, Science 289 (2000) 2291–2293.
[2] K. Takahashi, Iron oxide cluster induced barrier-free conversion of nitric oxide to ammonia, Chem. Commun. 51 (2015) 4062–4064.
[3] J.A. Rodriguez, T. Jirsak, G. Liu, J. Hrbek, J. Dvorak, A. Maiti, Chemistry of NO_2 on oxide surfaces: formation of NO_3 on TiO_2 (110) and $NO_2 \leftrightarrow$ O vacancy interactions, J. Am. Chem. Soc. 123 (2001) 9597–9605.
[4] L.B. Kreuzer, C.K.N. Patel, Nitric oxide air pollution: detection by optoacoustic spectroscopy, Science 173 (1971) 45–47.
[5] C.H. Kim, G.S. Qi, K. Dahlberg, W. Li, Strontium-doped perovskites rival platinum catalysts for treating NOx in simulated diesel exhaust, Science 327 (2010) 1624–1627.
[6] M. Shelef, Selective catalytic reduction of NOx with N-Free reductants, Chem. Rev. 95 (1995) 209–225.
[7] J.J. Yu, Z. Jiang, L. Zhu, Z.P. Hao, Z.P. Xu, Adsorption/Desorption studies of NOx on well-mixed oxides derived from Co-Mg/Al hydrotalcite-like compounds, J. Phys. Chem. B 110 (2006) 4291–4300.
[8] B. Xiao, P.S. Wheatley, X.B. Zhao, A.J. Fletcher, S. Fox, A.G. Rossi, L.L. Megson, S. Bardiga, L. Regli, K.M. Thomas, R.E. Morris, High-capacity hydrogen and nitric oxide adsorption and storage in a metal-organic framework, J. Am. Chem. Soc. 129 (2007) 1203–1209.
[9] L. Ma, J.H. Li, R. Ke, L.X. Fu, Catalytic performance characterization, and mechanism study of $Fe_2(SO_4)_3/TiO_2$ catalyst for selective catalytic reduction of NOx by ammonia, J. Phys. Chem. C 115 (2011) 7603–7612.
[10] Z.H. Ai, W.K. Ho, S.C. Lee, L.Z. Zhang, Efficient photocatalytic removal of NO in indoor air with hierarchical bismuth oxybromide nanoplate microspheres under visible light, Environ. Sci. Technol. 43 (2009) 4143–4150.
[11] A.L. Linsebigler, G.Q. Lu, J.T. Yates, Photocatalysis on TiO_2 surfaces: principles mechanisms, and selected results, Chem. Rev. 95 (1995) 735–758.
[12] M. Takeuchi, H. Yamashita, M. Matsuoka, M. Anpo, T. Hitao, N. Iton, Photocatalytic decomposition of NO under visible light irradiation on the Cr-ion-implanted TiO_2 thin film photocatalyst, Catal. Lett. 67 (2000) 135–137.
[13] Z.M. Liu, L.L. Ma, A.S.M. Junaid, NO and NO_2 adsorption on Al_2O_3 and Ga modified Al_2O_3 surfaces: a density functional theory study, J. Phys. Chem.: C 114 (2010) 4445–4450.
[14] M. Anpo, Y. Shioya, H. Yamashita, E. Giamello, C. Morterra, H. Che, S. Webber, S. Ouellette, Preparation and characterization of the Cu+/ZSM-5 catalyst and its reaction with NO under UV irradiation at 275 K. In situ photoluminescence EPR, and FT-IR investigations, J. Phys. Chem. 98 (1994) 5744–5750.
[15] Z.H. Ai, W.K. Ho, S.C. Lee, Efficient visible light photocatalytic removal of NO with BiOBr-graphene nanocomposites, J. Phys. Chem.: C 115 (2011) 25330–25337.
[16] F. Dong, W.K. Ho, S.C. Lee, Z.B. Wu, M. Fu, S.C. Zou, Y. Huang, Template-free fabrication and growth mechanism of uniform $(BiO)_2CO_3$ hierarchical hollow microspheres with outstanding photocatalytic activities under both UV and visible light irradiation, J. Mater. Chem. 21 (2011) 12428–12436.
[17] X. Ding, W.K. Ho, J. Shang, L.Z. Zhang, Self doping promoted photocatalytic removal of NO under visible light with Bi_2MoO_6: Indispensable role of superoxide ions, Appl. Catal. B: Environ. 182 (2016) 316–325.
[18] Z.H. Ai, L.Z. Zhang, S.C. Lee, Efficient visible light photocatalytic oxidation of NO on aerosol flow-synthesized nanocrystalline $InVO_4$ hollow microspheres, J. Phys. Chem.: C 114 (2010) 18594–18600.
[19] J.Z. Ma, C.X. Wang, H. He, Enhanced photocatalytic oxidation of NO over g-C_3N_4-TiO_2 under UV and visible light, Appl. Catal. B: Environ. 184 (2016) 28–34.
[20] G.H. Dong, L.P. Yang, F. Wang, L. Zang, C.Y. Wang, Removal of nitric oxide through visible light photocatalysis by g-C_3N_4 modified with perylene imides, ACS Catal. 6 (2016) 6511–6519.
[21] X.C. Wang, K. Maeda, A. Thomas, K. Takanabe, G. Xin, J.M. Carlsson, K. Domen, M. Antonietti, A metal-free polymeric photocatalyst for hydrogen production from water under visible light, Nat. Mater. 8 (2009) 76–80.
[22] G.H. Dong, W.K. Ho, L.Z. Zhang, Facile synthesis of porous graphene-like carbon nitride ($C_6N_9H_3$) with excellent photocatalytic activity for NO removal, Appl. Catal. B: Environ. 174-175 (2015) 477–485.
[23] Y.H. Li, L.P. Yang, G.H. Dong, W.K. Ho, Mechanism of NO photocatalytic oxidationon g-C_3N_4 was changed by Pd-QDs modification, Molecules 21 (2016) 36.
[24] Q.P. Wu, R.V.D. Krol, Selective photoreduction of nitric oxide to nitrogen by nanostructured TiO_2 photocatalysts: role of oxygen vacancies and iron dopant, J. Am. Chem. Soc. 134 (2012) 9369–9375.
[25] G.H. Dong, W.K. Ho, C.Y. Wang, Selective photocatalytic N_2 fixation dependent on g-C_3N_4 induced by nitrogen vacancies, J. Mater. Chem. A 3 (2015) 23435–23441.
[26] S.N. Li, G.H. Dong, R. Hailili, L.P. Yang, Y.X. Li, F. Wang, Y.B. Zeng, C.Y. Wang, Effective photocatalytic H_2O_2 production under visible light irradiation at g-C_3N_4 modulated by carbon vacancies, Appl. Catal. B: Environ. 190 (2016) 26–35.
[27] H. Li, J. Shang, Z.H. Ai, L.Z. Zhang, Efficient visible light nitrogen fixation with BiOBr nanosheets of oxygen vacancies on the exposed {001} facets, J. Am. Chem. Soc. 137 (2015) 6393–6399.
[28] K. Zhao, L.Z. Zhang, J.J. Wang, Q.X. Li, W.W. He, J.J. Yin, Surface structure-dependent molecular oxygen activation of BiOCl single-crystalline nanosheets, J. Am. Chem. Soc. 135 (2013) 15750–15753.
[29] Y.H. Wu, B. Yuan, M.R. Li, W.H. Zhang, Y. Liu, C. Li, Well-defined BiOCl colloidal ultrathin nanosheets: synthesis, characterization, and application in photocatalytic aerobic oxidation of secondary amines, Chem. Sci. 6 (2015) 1873–1878.
[30] W.L. Yang, L. Zhang, J.F. Xie, X.D. Zhang, Q.H. Liu, T. Yao, S.Q. Wei, Q. Zhang, Y. Xie, Enhanced photoexcited carrier separation in oxygen-doped $ZnIn_2S_4$ nanosheets for hydrogen evolution, Angew. Chem. Int. Ed. 55 (2016) 6716–6720.
[31] G.H. Dong, Z.H. Ai, L.Z. Zhang, Efficient anoxic pollutant removal with oxygen functionalized graphitic carbon nitride under visible light, RSC Adv. 4 (2014) 5553–5560.
[32] Z.J. Wang, S. Ghasimi, K. Landfester, K.A.I. Zhang, Molecular structural design of conjugated microporous poly (Benzooxadiazole) networks for enhanced photocatalytic activity with visible light, Adv. Mater. 27 (2015) 6265–6270.
[33] L. Wang, X.Z. Jiang, Plasma-induced reduction of chromium (VI) in an aqueous solution, Environ. Sci. Technol. 42 (2008) 8492–8497.
[34] S.C. Yan, Z.S. Li, Z.G. Zou, Photodegradation of rhodamine B and methyl orange over boron-doped g-C_3N_4 under visible light irradiation, Langmuir 26 (2010) 3894–3910.
[35] T.T. Zhang, W.Y. Lei, P. Liu, J.A. Rodriguez, J.G. Yu, Y. Qi, G. Liu, M.H. Liu, Organic pollutant photodecomposition by Ag/$KNbO_3$ nanocomposites: a combined experimental and theoretical study, J. Phys. Chem. C 120 (2012) 2777–2788.
[36] L. Wang, M.H. Cao, Z.H. Ai, L.Z. Zhang, Dramatically enhanced aerobic atrazine degradation with Fe@Fe_2O_3 core-shell nanowires by tetrapolyphosphate, Environ. Sci. Technol. 48 (2014) 3354–3362.
[37] X.J. Liu, D.X. Tian, S.Z. Ren, C.G. Meng, Structure sensitivity of NO adsorption-dissociation on Pd n (n = 8, 13, 19, 25) clusters, J. Phys. Chem. C 119 (2015) 12941–12948.
[38] Z.H. Wang, W.H. Ma, C.C. Chen, J.C. Zhao, Probing paramagnetic species in titania-based heterogeneous photocatalysis by electron spin resonance (ESR) spectroscopy-a mini review, Chem. Eng. J. 170 (2011) 353–362.
[39] J.H. Lunsford, ESR of adsorbed oxygen species, Cat Rev. 8 (1973) 135–157.